Helmholtz-Zentrum Dresden-Rossendorf (HZDR)

HZDR
HELMHOLTZ ZENTRUM
DRESDEN ROSSENDORF

A tailored 100%-efficient 532/1064-nm demultiplexer in y-cut LiNbO3 crystal

Liu, H.; Li, Y.; Yang, Q.; Zhou, S.; Jia, Y.;

Originally published:

January 2023

Optics Letters 48(2023), 787-790

DOI: https://doi.org/10.1364/OL.480495

Perma-Link to Publication Repository of HZDR:

https://www.hzdr.de/publications/Publ-36872

Release of the secondary publication
on the basis of the German Copyright Law § 38 Section 4.

A tailored 100%-efficient 532/1064-nm demultiplexer in *y*-cut $LiNbO_3$ crystal

Hongliang Liu[1,2], Yuanbo Li[1], Quanxin Yang[1], Shengqiang Zhou[3], and Yuechen Jia[2]

1 Tianjin Key Laboratory of Micro-Scale Optical Information Science and Technology, Institute of Modern Optics, Nankai University, Tianjin 300350, China

2 School of Physics, State Key Laboratory of Crystal Materials, Shandong University, Jinan 250100, China

3 Helmholtz-Zentrum Dresden-Rossendorf, Institute of Ion Beam Physics and Materials Research, Dresden 01328, Germany

*Corresponding author: drliuhl@nankai.edu.cn

Abstract

In this Letter, we report a tailored 532/1064-nm demultiplexer based on a multimode interference (MMI) coupler with an efficiency of 100%. The device structure is designed according to the self-imaging principle, and the propagation and the wavelength division performance are simulated by the beam propagation method. The demultiplexer is fabricated in a *y*-cut $LiNbO_3$ crystal by femtosecond laser direct writing (FLDW) combined with the ion implantation technique. The end-face coupling system is used to measure the near field intensity distribution, and the spectra collected from the output ports are obtained by spectrometers. The simulated and the experimental results indicate that the customized demultiplexer in the $LiNbO_3$ crystal presents excellent wavelength division performance operating at 532 nm and 1064 nm. This work demonstrates the application potential of FLDW technology for developing miniaturized photonic components and provides a new strategy for fabricating high-efficiency integrated wavelength division devices on an optical monocrystalline platform.

In recent years, the integration of waveguide devices on an optical monocrystal chip has attracted increasing interest [1]. As a crystalline material, lithium niobate ($LiNbO_3$) has been widely used in fabricating integrated optical devices such as beam splitters [2], optical switches [3], electro-optical modulators [4,5], and optical resonators [6,7] due to its good physical and chemical stability, low-optical loss, high-electro-optical coefficients, and excellent nonlinear optical properties [8,9]. An optical waveguide, which is one of the fundamental elements of integrated optics, can be used to combine with other devices with different functions or designs [10]. Among the several ways to fabricate optical waveguides in optical materials, the irradiation of swift heavy ions is a powerful and effective technique with many advantages including the reduced irradiation fluences, large refractive index modification, and faster fabrication processing [11]. In addition, femtosecond laser direct writing (FLDW) shows great potential due to the unique features of flexible 3D micro-/nano-fabrication configurations and efficiency, and ease to use [12,13]. By using ion implantation combined with FLDW, several photonic devices have been proposed, such as *Q* switched lasers based on the ridge waveguide [14], beam splitters [15,16], photodiodes [17], and quantum nano-devices [18].

A demultiplexer often plays a key role in the integrated optical circuit as a special beam splitter, which is always applied to realize wavelength division [19]. Based on different platforms,

several devices have been designed to perform this function including Y-branch devices [20], Mach–Zehnder interferometers [21,22], multimode interference (MMI) couplers [23,24], arrayed waveguide de-multiplexers [25], and angled MMI-based de-multiplexers [26,27]. Additionally, with the MMI structure, the device shows several outstanding advantages including a simple and compact structure, good fabrication tolerance, and ease to achieve 1 × N splitting [28]. However, the operating wavelength of most demultiplexers introduced in previous works is concentrated in the infrared spectral range. In addition, most of them are fabricated by way of UV lithography combined with ion beam etching [29], a focused ion beam [30], or electron-beam lithography [31–33], which are relatively complicated compared to FLDW. In this work, we have fabricated an MMI-based demultiplexer by FLDW combined with swift carbon ion irradiation in a y-cut $LiNbO_3$ crystal with the working wavelength at 532/1064 nm. The device structure has been designed and the distribution of the output optical field performances has been theoretically simulated by the beam propagation method (BPM). The near-field distribution and the spectra collected from the output ports have been obtained by the CCD camera and spectrometers, respectively. Excellent single-mode distribution and wavelength division features for the tailored demultiplexer have been demonstrated at wavelengths of 532 nm and 1064 nm.

As shown in Fig. 1, the wavelength demultiplexer consists of three parts: an input port (Port 1), two output ports (Port 2, Port 3), and an MMI coupler. The demultiplexer based on the MMI is designed by the self-imaging effect, which exists in the multimode waveguide. According to the self-imaging principle [34], the incident laser propagates along the waveguide direction, and the image can be reproduced by the interference between waveguide modes at specific locations (periodic intervals). The periodic properties of imaging depend both on the input field and the MMI structure, which can be defined as the beat length L_π of the two lowest-order modes:

$$L_\pi = \frac{\pi}{\beta_0 - \beta_1} \simeq \frac{4n_{eff}W_e^2}{3\lambda},$$

where β_0 and β_1 are the propagation constants of the two lowest-order modes, n_{eff} is the effective index of the waveguide in the interference region, and W_e is the effective width of the multimode interference region, which is similar to the width of the MMI structure. Here, λ is the free-space wavelength of the input field.

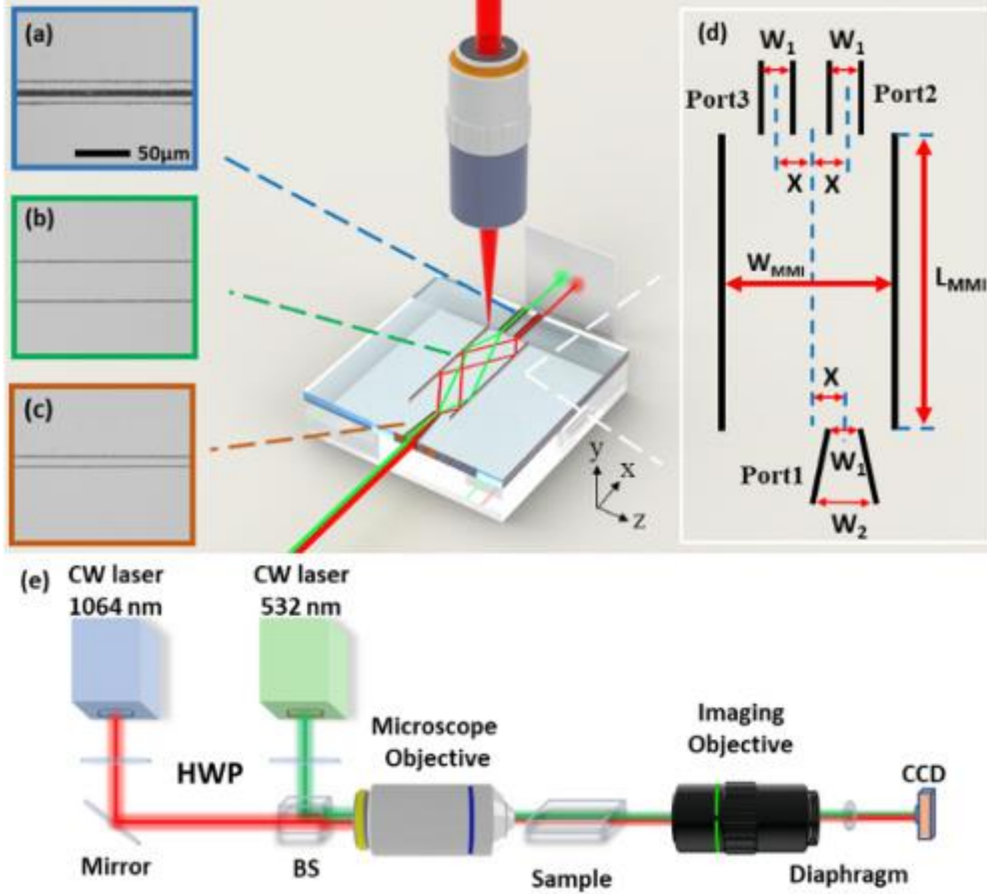

Fig. 1. Schematic illustration of the demultiplexer based on the MMI structure. (a) Micrograph of the output port region; (b) micrograph of the MMI coupler region; (c) micrograph of the input port region. (d) Schematic diagram of the designed demultiplexer. The input port is Port 1, the output ports are Port 2 and Port 3, and the mid part is the MMI coupler. (e) Schematic illustration of the laser-coaxial end-face coupling system.

For the input light fields at different wavelengths, they possess different beat lengths. When the length of the multimode waveguide is an even/odd multiple of the beat length, a direct/mirrored single image will be symmetrically formed on both sides of the center of the MMI waveguide structure. According to this principle, a suitable length of the MMI structure can realize wavelength division of the input fields, the length L_{MMI} can be calculated as

$$L_{\text{MMI}} = pL_{\pi}^{\lambda_1} = (p+q)L_{\pi}^{\lambda_2}, \text{with } p = 0, 1, 2,$$

where q is a positive odd integer, and $L\lambda\pi$ is the beat length corresponding to the wavelength λ. In this case, the input and output ports should be located at $\pm W_{MMI}/6$ from the center of the MMI coupler by the restricted interference mechanisms [34].

The demultiplexer is fabricated on a y-cut $LiNbO_3$ crystal with a size of $10 \times 10 \times 2$ mm^3, which is optically polished. An ion implantation layer with a depth of 10 μm is formed on the x–z facet by swift heavy C^{5+} ion beam irradiation with an energy of 16 MeV, a fluence of 3×10^{14} ions/cm^2, and an incident angle of 7°. The ion beam is generated by the 3-MV tandem accelerator at Helmholtz-Zentrum Dresden-Rossendorf, Germany. In the projected range of the incident C^{5+} ions, a positive index well in the near-surface region and a negative optical barrier

at the end of the incident ion track have been formed during the irradiation, which is similar to the previous report [35]. Therefore, a low-loss planar waveguide with a typical “well + barrier” index distribution will be formed through the ion implantation, and the width of the guiding region is approximately 6 μm. Then, the device is fabricated by using an amplified Ti:sapphire laser system (Astrella, Coherent Inc., USA), which generates a laser beam with a 1-kHz repetition rate, 40-fs pulse width, 6-mJ pulse energy, and the center wavelength at 800 nm. The pulse energy can be adjusted by a wall pilot motorized attenuator and the sample is placed on a six-dimensional motorized stage. Figures 1(a)–1(c) illustrate the micrographs of the input ports, the MMI coupler, and the output port. During the fabrication process, the energy of the laser is set to 41 μJ, and the speed of the motorized stage is set to 0.1 mm/s. The sides of the waveguide and the MMI structure have been direct written through moving the sample as the designed configuration. A slight modification of reducing the refractive index would be induced at the direct writing regions. Finally, a square cladding waveguide has been formed.

The BPM is used to simulate the propagation of the input field inside the waveguide. Here, we build a 3D model according to the structure shown in Fig. 1(d). To facilitate subsequent femtosecond laser processing and waveguide characterization, the input port is designed to be tapered, which will also improve the coupling performance. The W_{MMI}, W_1, and W_2 values are set to be 36 μm, 7 μm, and 12 μm, respectively. The X is set to be 6 μm, two monitors are placed at ±X to detect the changes of the input field intensity. According to the principle of birefringence, the incident fields with linearly polarization states (i.e., TE and TM; TE, the electric field is parallel to the z axis; TM, parallel to the y axis) correspond to n_e and n_o within the crystal, respectively. For the y-cut $LiNbO_3$, the n_e is 2.234 at the wavelength of $\lambda_1 = 532$ nm and the n_o is 2.232 at the wavelength of $\lambda_2 = 1064$ nm. Obviously, the $n_{\lambda 1e}$ and $n_{\lambda 2o}$ are approximately equivalent, and it can be calculated that $L_{\lambda 1\pi} \approx 2L_{\lambda 2\pi}$ by Eqs. (1) and (2) under this circumstance. Due to the value difference of $n_{\lambda 2e}$ (~2.156) and $n_{\lambda 1o}$ (~2.323), it is inaccessible to realize a compact-size and high-performance device with the 532-nm laser at TM polarization and the 1064-nm one at TE polarization. Thus, we fix the length L_{MMI} to be 7350 μm, and Gaussian beams at wavelengths of $\lambda_1 = 532$ nm (TE polarization) and $\lambda_2 = 1064$ nm (TM polarization) are used as the laser source. Figures 2(a) and 2(c) illustrate the propagation of the input field in the simulation structure. In Fig. 2(a), the incident laser field is the fundamental mode of the Gaussian beam at 532 nm (TE), and is reproduced near Port 3 and output along the waveguide Port 3. Figure 2(b) shows the changes of the field intensity in the direction of the two monitors, with most of the laser is coupled into Port 3. The propagation loss is calculated to be 0.17 dB/cm according to the simulation results. In Fig. 2(c), the input field is the fundamental mode of the Gaussian beam at 1064 nm (TM), and is reproduced near Port 2 and output along the waveguide. Similarly, the specific distribution of the field intensity can be seen in Fig. 2(d). In this case, most of laser is coupled into Port 2, and the propagation loss is calculated to be 0.27 dB/cm.

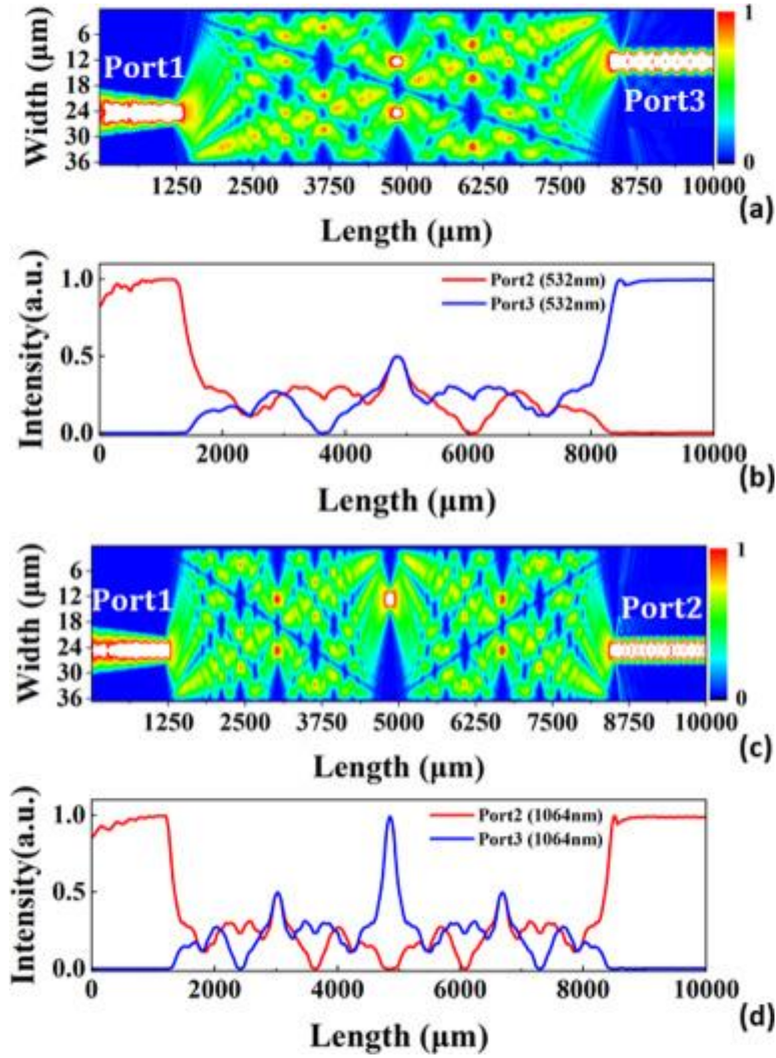

Fig. 2. (a) and (c) Simulations of the input fields propagating in the waveguide under the operating wavelength at 532 nm and 1064 nm, respectively. (b) and (d) Intensity of the optical field at the lines of two monitors under the operating wavelength at 532 nm and 1064 nm, respectively.

Then, we studied the transmission performance of the fabricated structure. A laser-coaxial end-face coupling system has been used to measure the intensity distribution of the output optical field, as shown in Fig. 1(e). Two CW lasers at wavelengths of 532 nm and 1064 nm are tuned for coaxial incidence by a plane mirror and a beam splitter prism. Two half-wave plates are used to adjust the polarization of the incident laser. Then the beam is coupled into the incident waveguide through the microscope objective (40×, N.A. = 0.65) and the output laser is finally imaged on the CCD camera through an imaging objective (50×, N.A. = 0.42). Figure 3 shows the images captured by the CCD, and the output modal profiles are shown to exhibit single-mode features. When the 532-nm and 1064-nm lasers are incident at the same time, the two laser beams can be observed on the CCD as shown in Figs. 3(a) and 3(b), which correspond to the positions of the output Port 3 and Port 2, respectively. Figures 3(c) and 3(d) exhibit the 2D and 3D profiles of the laser intensity distribution when the applied incident laser is at 532 nm, and the output laser beam is located at Port 3. Similarly, if the incident laser is at 1064 nm, the output laser will be located at Port 2, as depicted in Figs. 3(e) and 3(f). These results are consistent with the previous simulation conclusions, and can prove that this device realizes the function of 100% separation of the 532-nm and 1064-nm lasers with polarization dependence. The insertion loss of this designed structure is calculated to be 7.5 dB and 10.8 dB at the wavelength of 532

nm and 1064 nm, respectively. The relatively large losses are mainly caused by the fabrication error at the connection parts of the device and the coupling losses.

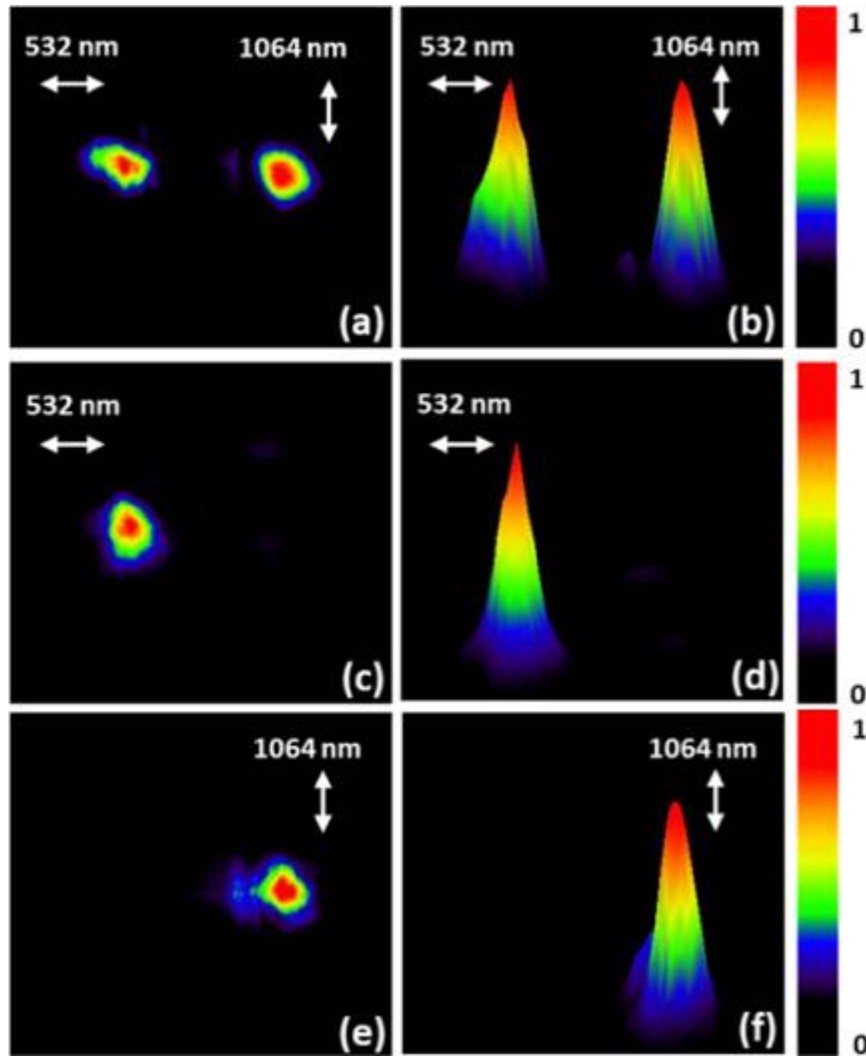

Fig. 3. Intensity distribution of the output optical field measured by the CCD. (a) and (b) 2D and 3D images corresponding to the simultaneous coaxial input of 532-nm (TE) and 1064-nm (TM) laser; (c) and (d) 2D and 3D images when the incident field is only a 532-nm (TE) laser; (e) and (f) 2D and 3D images when the incident field is only a 1064-nm (TM) laser.

The optical spectrum is further measured by two fiber spectrometers: the NOVA-EX and the NIR2500 based on one Y-branch optical fiber probe. Figure 4 illustrates the spectra at the position of Port 2 and Port 3 when applying incident lasers at different wavelengths, separately. As the green and brown lines show in Fig. 4, a spectral signal at 532 nm has been detected in the position of Port 3 when the incident laser is at 532 nm. However, there is no significant signal near the Port 2 when we measured through changing the position of the fiber probe. The red and orange lines depict that a spectral signal can be found at 1064 nm only in the position of Port 2 when the 1064-nm laser was applied. When the 532-nm and 1064-nm lasers are incident at the same time, two spectral signals at 532 nm and 1064 nm can be detected at the positions of Port 2 and Port 3 separately, which is shown by the cyan line and the blue line. The results measured by the spectrometers verify that the wavelengths of the laser output collected from the two ports in different cases are in accordance with the previous simulation and coupling results. It can be found that excellent wavelength division performance has been achieved by comparing the intensity of the spectra in different output ports with the same incident optical field in the above cases.

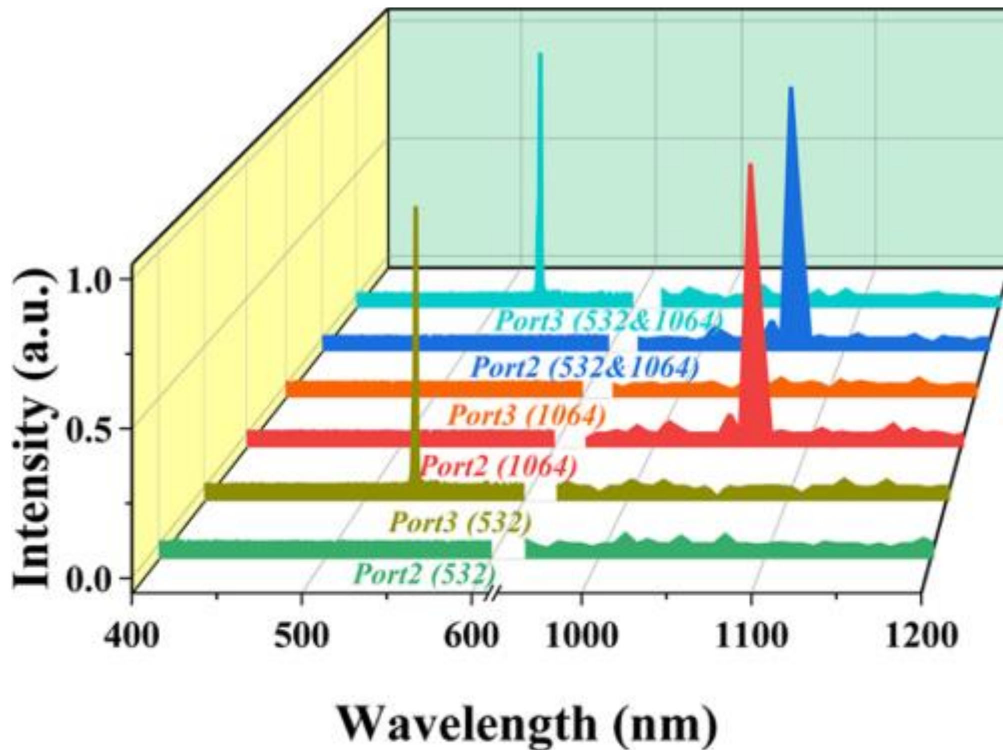

Fig. 4. Spectra at the positions of Port 2 and Port 3 with different incident lasers.

In conclusion, we report a tailored 532/1064-nm wavelength demultiplexer based on an MMI coupler, which is fabricated by FLDW in a y-cut $LiNbO_3$ crystal based on C^{5+} ions implantation. According to the self-imaging principle, the dimension of the device is designed with a compact size. The results of the theoretical simulations and the experimental investigations show that the demultiplexer achieves a nearly 100% efficient wavelength division performance with a polarization dependence at the operating wavelengths. By optimizing the size of the structure and processing parameters, the insertion loss of the device can be further reduced. Due to the specificity of the operating wavelength and the nonlinear characteristics of the crystal, this tailored structure also has the potential to work as an active device for second harmonic generation with pumping by a pulsed 1064-nm laser. It is worth noting that a wide range of operating wavelengths can also be achieved by changing the crystals and parameters of the structure. Thus, it shows great potential that our design and processing methods can be applied to the fabrication of on-chip demultiplexer devices in the future.

Funding

National Natural Science Foundation of China (12074223, 12104256, 12134009, 12274236).

REFERENCES

1. Y. Jia, S. Wang, and F. Chen, Opto-Electron. Adv. **3**, 190042 (2020). [CrossRef]

2. B. Wu, B. Zhang, W. Liu, Q. Lu, L. Wang, and F. Chen, Opt. Laser Technol. **145**, 107500 (2022). [CrossRef]

3. Q. Guo, R. Sekine, L. Ledezma, R. Nehra, D. J. Dean, A. Roy, R. M. Gray, S. Jahani, and A. Marandi, Nat. Photonics **16**, 625 (2022). [CrossRef]

4. C. Wang, M. Zhang, X. Chen, M. Bertrand, A. Shams-Ansari, S. Chandrasekhar, P. Winzer, and M. Loncar, Nature **562**, 101 (2018). [CrossRef]

5. M. Jin, J. Chen, Y. Sua, P. Kumar, and Y. Huang, Opt. Lett. **46**, 1884 (2021). [CrossRef]

6. Y. Xu, M. Shen, J. Lu, J. B. Surya, A. A. Sayem, and H. X. Tang, Opt. Express **29**, 5497 (2021). [CrossRef]

7. M. Zhang, C. Wang, R. Cheng, A. Shams-Ansari, and M. Lončar, Optica **4**, 1536 (2017). [CrossRef]

8. D. Sun, Y. Zhang, D. Wang, W. Song, X. Liu, J. Pang, D. Geng, Y. Sang, and H. Liu, Light: Sci. Appl. **9**, 197 (2020). [CrossRef]

9. J. Lin, F. Bo, Y. Cheng, and J. Xu, Photonics Res. **8**, 1910 (2020). [CrossRef]

10. P. Wu, S. Yang, Y. Ren, and H. Liu, Front. Phys. **9**, 719757 (2021). [CrossRef]

11. S. He, Z. Zhang, H. Liu, S. Akhmadaliev, S. Zhou, X. Wang, and P. Wu, Appl. Phys. Express **12**, 076502 (2019). [CrossRef]

12. Q. Yang, H. Liu, S. He, Q. Tian, B. Xu, and P. Wu, Opto-Electron. Adv. **4**, 200005 (2021). [CrossRef]

13. Y. Zhuang, S. Wang, Z. Chen, Y. Jia, W. Zhang, Y. Yao, Y. Ren, F. Chen, and H. Liu, Appl. Phys. Lett. **120**, 211101 (2022). [CrossRef]

14. S. Wang, X. Sun, Y. Jia, and F. Chen, Opt. Laser Technol. **145**, 107540 (2022). [CrossRef]

15. Y. Yao, W. Wang, and B. Zhang, Opt. Express **26**, 19648 (2018). [CrossRef]

16. C. Chen, S. Akhmadaliev, C. Romero, J. R. V. de Aldana, S. Zhou, and F. Chen, J. Lightwave Technol. **35**, 225 (2017). [CrossRef]

17. C.-H. Li, J.-H. Zhao, X.-Y. Yu, Q.-D. Chen, J. Feng, P.-D. Han, and H.-B. Sun, IEEE Sens. J. **17**, 2367 (2017). [CrossRef]

18. S. M. Eaton, J. P. Hadden, V. Bharadwaj, J. Forneris, F. Picollo, F. Bosia, B. Sotillo, A. N. Giakoumaki, O. Jedrkiewicz, A. Chiappini, M. Ferrari, R. Osellame, P. E. Barclay, P. Olivero, and R. Ramponi, Adv. Quantum Technol. **2**, 1900006 (2019). [CrossRef]

19. M. Koshiba, J. Lightwave Technol. **19**, 1970 (2001). [CrossRef]

20. A. Rostami, H. A. Banaei, F. Nazari, and A. Bahrami, Optik **122**, 1481 (2011). [CrossRef]

21. Z. Zhao, Z. Li, J. Niu, G. Zhang, H. Chen, X. Fu, and L. Yang, Photonics **9**, 252 (2022). [CrossRef]

22. L. Xu, Y. Wang, D. Mao, E. El-Fiky, Z. Xing, A. Kumar, M. G. Saber, M. Jacques, and D. V. Plant, Opt. Lett. **44**, 1770 (2019). [CrossRef]

23. Y. E. Marin, A. Celik, S. Faralli, L. Adelmini, C. Kopp, F. D. Pasquale, and C. J. Oton, J. Lightwave Technol. **37**, 4770 (2019). [CrossRef]

24. M. S. Rouifed, C. G. Littlejohns, G. X. Tina, H. Qiu, J. S. Penades, M. Nedeljkovic, Z. Zhang, C. Liu, D. J. Thomson, G. Z. Mashanovich, G. T. Reed, and H. Wang, Opt. Express **25**, 10893 (2017). [CrossRef]

25. A. Malik, M. Muneeb, S. Pathak, Y. Shimura, J. Van Campenhout, R. Loo, and G. Roelkens, IEEE Photonics Technol. Lett. **25**, 1805 (2013). [CrossRef]

26. E. Ioudashkin and D. Malka, Nanomaterials **10**, 2338 (2020). [CrossRef]

27. J. Zhang, L. Han, B. P.-P. Kuo, and S. Radic, J. Lightwave Technol. **38**, 5748 (2020). [CrossRef]

28. L. Nikolaevsky, T. Shchori, and D. Malka, IEEE Photonics Technol. Lett. **30**, 720 (2018). [CrossRef]

29. Y. Chen, S. Wu, J. Zhang, M. Zhu, and J. Xiao, Opt. Laser Technol. **153**, 108290 (2022). [CrossRef]

30. F. Li, Z. Y. Yang, J. J. Shi, and X. B. He, Opt. Express **30**, 37753 (2022). [CrossRef]

31. H. Xu, L. Liu, and Y. Shi, Opt. Lett. **43**, 1483 (2018). [CrossRef]

32. F. Beutel, F. Brückerhoff-Plückelmann, H. Gehring, V. Kovalyuk, P. Zolotov, G. Goltsman, and W. H. P. Pernice, Optica **9**, 1121 (2022). [CrossRef]

33. S. Chen, Z. Xie, H. Ye, X. Wang, Z. Guo, Y. He, Y. Li, X. Yuan, and D. Fan, Light: Sci. Appl. **10**, 222 (2021). [CrossRef]

34. L. B. Soldano and E. C. Pennings, J. Lightwave Technol. **13**, 615 (1995). [CrossRef]

35. F. Chen, Y. Tan, and A. Ródenas, Opt. Express **16**, 16209 (2008). [CrossRef]